Improved finite-source inversion through joint measurements of rotational and translational ground motions: A theoretical study

Michael Reinwald[1], Moritz Bernauer[2], Heiner Igel[2], and Stefanie Donner[2]

[1]Laboratoire d'Imagerie Biomédicale, UPMC, Paris, France
[2]Department of Earth and Environmental Sciences, LMU Munich, Munich, Germany
Correspondence to: Michael Reinwald (mchlrnwld@gmail.com)

Abstract. With the prospects of seismic equipment being able to measure rotational ground motions in a wide frequency and amplitude range in the near future we engage in the question how this type of ground motion observation can be used to solve the seismic inverse problem. In this paper, we focus on the question, whether finite source inversion can benefit from additional observations of rotational motion. Keeping the overall number of traces constant, we compare observations from a surface seismic network with 44 3-component translational sensors (classic seismometers) with those obtained with 22 6-component sensors (with additional 3-component rotational motions). Synthetic seismograms are calculated for known finite-source properties. The corresponding inverse problem is posed in a probabilistic way using the Shannon information content as measure how the observations constrain the seismic source properties. We minimize the influence of the source receiver geometry around the fault by statistically analyzing six-component (three velocity and three rotation rate) inversions with a random distribution of receivers. The results show that with the 6-C subnetworks the source properties are not only equally well recovered (even that would be benefitial because of the substantially reduced logistics installing half the sensors) but statistically some source properties are almost always better resolved. We assume that this can be attributed to the fact that the (in particular vertical) gradient information is contained in the additional motion components. We compare these effects for strike-slip and normal-faulting type sources and confirm that the increase in inversion quality for kinematic source parameters is even higher for the normal fault. This indicates that the inversion benefits from the additional information provided by the horizontal rotation rates, i.e. information about the vertical displacement gradient.

Keywords: Inverse theory, Rotational seismology, finite source earthquakes, bayesian inversion

1 Introduction

The inversion for kinematic finite source models of earthquakes plays an important role in the research of earthquake dynamics and the general understanding of earthquakes. Finite source inversion of earthquakes is non-unique due to noisy data, sparse geographical coverage of seismic stations, the non-linearity of the forward problem and possible unrealistic simplifications in the parametrization of the fault.

According to classical elasticity theory, if $\boldsymbol{u}(\boldsymbol{x})$ is the displacement of a particle at position x and if deformation is considered

to be infinitesimal, the displacement of a particle at position $\boldsymbol{u}(\boldsymbol{x}+\delta\boldsymbol{x})$ can be described with the following equation (Aki and Richards, 2002):

$$\boldsymbol{u}(\boldsymbol{x}+\delta\boldsymbol{x}) = \boldsymbol{u}(\boldsymbol{x}) + \boldsymbol{\epsilon} \cdot \delta\boldsymbol{x} + \boldsymbol{\omega} \times \delta\boldsymbol{x} \tag{1}$$

In Equation 1, ϵ is the symmetric strain tensor, therefore containing six instead of nine independent components, and $\boldsymbol{\omega} = (\frac{1}{2}\nabla \times \boldsymbol{u})$ are the rotations around each of the three translational axes of $\boldsymbol{u}$. Therefore the full description of a displacement around a point x needs three translational, three rotational and six strain components. The rotation components are mathematically related to the space derivatives of the translational motion components u_x, u_y, u_z:

$$\begin{pmatrix} \omega_x \\ \omega_y \\ \omega_z \end{pmatrix} = \frac{1}{2} \begin{pmatrix} \partial_x \\ \partial_y \\ \partial_z \end{pmatrix} \times \begin{pmatrix} u_x \\ u_y \\ u_z \end{pmatrix} = \frac{1}{2} \begin{pmatrix} \partial_y u_z - \partial_z u_y \\ \partial_z u_x - \partial_x u_z \\ \partial_x u_y - \partial_y u_x \end{pmatrix} \tag{2}$$

Although rotational ground motions are caused by earthquake source processes, measurements thereof have not been carried out until the 1990s (Nigbor, 1994; Takeo, 1998). Nevertheless, the possible benefit has been considered decades before - in the first edition of Aki and Richards, 2002, which was published in 1980. Even then, the methods that were used mostly consisted of several three-component seismometers and were not able to be used for seismology because of their low sensitivity (Suryanto, 2006). Since then, many scientists commended the benefits of studying rotational ground motions for earth sciences (Twiss et al., 1993; Spudich et al., 1995; Takeo and Ito, 1997; Igel et al., 2007; Fichtner and Igel, 2009), physics (DeSalvo, 2009; Lantz et al., 2009) and also for engineering applications (Trifunac, 2009). In the last years, new instruments, e.g. ring-laser technology (Schreiber et al., 2009; Velikoseltsev et al., 2012) or adapted gyroscopes (Bernauer et al., 2012), that are capable of measuring rotational motions with a much higher precision, have been developed and possibly bring new insight into seismological applications.

With the potential availability of seismometers measuring rotational ground motions, the goal of this study is to test the effect of incorporating rotational ground motion data into finite source inversions for different fault mechanisms. Following the approach by (Bernauer et al., 2014), we employ a Bayesian, i.e. probabilistic, inversion algorithm and compare the inversions with different data types and different earthquake source mechanisms. In the last decade there have been several studies showing that probabilistic methods are well suited for ill-posed inversion problems of finite source earthquakes, because they overcome the drawbacks of regularization techniques such as local minima ((Monelli et al., 2009; Fichtner and Tkalčić, 2010)).

We directly compare the results with and without incorporation of rotational ground motion data for a pure strike-slip earthquake and for a dip-slip earthquake, i.e. the strike also propagates in vertical direction. Because rotations around the horizontal axes (i.e. ω_x and ω_y in Equation (2)) carry information about vertical gradients, which is not possible to resolve with common arrays on the Earth's surface (Bernauer et al., 2014), we expect to see an even greater benefit for inversions for the dip-slip scenario due to the higher energy in the horizontal rotation components.

To better assess the quality differences we keep the number of seismograms used in the inversion the same for all scenarios. Because using three translational and three rotational ground motion recordings doubles the amount of seismograms, we half the number of seismic stations when using the so-called 6C (six-component) data, as compared to only three translational seismograms (3C/three-component data). In the following chapter, we present the Bayesian inversion scheme. Next, we explain the

5   parametrization of the synthetic earthquakes, the spatial distribution of the seismic stations and define the different inversion scenarios. We will then present the inversion results with and without incorporation of the rotational ground motion data for the two different earthquake mechanisms.

2   Probabilistic Inversion Scheme

10   Although computation time is drastically increased when applying probabilistic inversion schemes, it avoids drawbacks such as regularization or falling into local minima in the iterations during the process of minimizing the misfit between model and data. We use the basic ideas of bayesian inversion for a finite fault developed by (Tarantola, 2005) and (Mosegaard and Tarantola, 1995): For each inversion, a certain number of parameters is stored in the vector $\boldsymbol{m}$, given by

$$\sigma(\boldsymbol{m}) = \kappa \cdot \rho(\boldsymbol{m}) L(\boldsymbol{m}), \tag{3}$$

15   with the normalization constant κ and the associated probability density functions of the prior $\rho(\boldsymbol{m})$ and posterior probability $\sigma(\boldsymbol{m})$ on the model parameters $/vecm$. $L(\boldsymbol{m})$ is defined as the likelihood function, which features information about how well the model explains the data.

$$L(\boldsymbol{m}) = \kappa^{'} \cdot exp\left[-\sum(\frac{\chi_l(\boldsymbol{m})}{s_l})\right], \tag{4}$$

In Equation (4), $\kappa^{'}$ is again a normalization constant, $\chi_l(\boldsymbol{m})$ denotes the measure of misfit between the predicted model data

20   and the observed data and s_l represents the noise level.

The *prior pdf* $\rho(\boldsymbol{m})$ is set to be constant in all model parameters within a certain interval of interest. Since all model parameters are independent, the combined *prior pdf* can be obtained by simply multiplying the probability densities for all parameters. In order to calculate the *posterior pdf*, we let the probabilistic inversion do random walks through the entire model space. We approximate the *posterior pdf* for all 26 parameters by applying the Metropolis algorithm to $1,000,000$ test models. Once the

25   entire model space is sampled, one can illustrate it by marginal density distributions of each of the parameters. The shape of the these distributions gives a discrete approximation of the *posterior pdf*.

To quantify the *posterior pdf* compared to the *prior pdf*, i.e. the relative information gain, we use the so-called *Shannon's measure of information gain*:

The relative information gain $I(\rho;\sigma)$ with respect to the *posterior pdf* ρ and the *prior pdf* σ is defined in (Tarantola, 2005) as

$$I(\rho;\sigma) = \int \rho(x) log_2 \left[\frac{\rho(x)}{\sigma(x)} \right] dx. \tag{5}$$

Since the base of the logarithm in Equation 5 is 2, the unit of I is termed a bit. One major advantage of this method is the
5   possible comparison between results of very different experiments by quantification of the inversion quality. For further details on the method we refer to the publications of (Bernauer et al., 2014) and (Tarantola, 2005).

3   Forward Model

The generation of the databases, in which the Green's functions are stored, is done with the program Instaseis (van Driel et al., 2015), based on the parallel spectral-element method AxiSEM (Nissen-Meyer et al., 2014), which allows for near instantaneous
10   (on the order of milliseconds) extraction of seismograms. We used the velocity model ak135f in out simulations (Kennett et al., 1995).

We illustrate receiver and fault setup in Figure 1. 44 Receivers, marked as grey, and red triangles, are setup around the source with a spacing of $0.4°$ latitude and $0.25°$ longitude to guarantee a good coverage in all directions from the fault. Since we want to decrease the number of receivers by a factor of 2 when incorporating rotational ground motion data to keep the amount of
15   data used in the inversion the same, we will limit our recording to the 22 stations marked with red triangles, when using both data types. The fault, illustrated as a black line, has a constant latitude of $0°$ and the epicenter of the earthquake is marked with a yellow star. At this point we want to emphasize that due to the theoretical nature of this study the geographical location of fault and receivers are in no way related to real data of past earthquakes or geographical areas.

We brake up the fault plane into $8 \cdot 3 = 24$ quadratic subfaults. Each subfault is filled by $8 \cdot 8 = 64$ moment tensor point sources
20   with a regular spacing of 500 meters between the point sources. The side-length of each subfault is therefore about 4km. We illustrate the fault in a 2D sketch shown in Figure 2. All of the moment tensor point sources are illustrated by small black dots and the subfaults are patterned in a gray/white color scheme for easier distinction of the subfaults. We set the hypocenter - marked as a yellow star - to be exactly between four subfaults. The parametrization of the fault and the rupture itself is used in the same manner as in (Bernauer et al., 2014): We allow each subfault to slip once, with a delay of the average time of all
25   rupture times of the 64 point sources in the subfault. This is calculated with a homogeneous rupture velocity $c^{rup} = 2700$ m/s across the entire fault and the computed distances of each point source. The second parameter is the rise time (R) which is also homogeneous for the entire fault. It expresses the duration of the slip and is incorporated in the source time function used for the forward modeling. We choose the source time function to be an ordinary ramp function. The third parameter that contributes to the seismic response is the final slip amplitude. This parameter is defined for all subfaults individually. The complete seismic
30   response $v_r(\omega)$ at station r in the frequency domain, with circular frequency $\omega = 2\pi f$ and summed over all subfaults k, is

expressed in Equation 6. Note that there are two parameters (i.e. rupture velocity and rise time) that are not linearly related to displacement or velocity, contrary to the 24 slip amplitudes. We therefore invert for 26 kinematic source parameters.

$$v_r(\omega) = \sum_{k=1}^{N} slip_k \cdot exp\left[-i\omega t_k(c^{rup})\right] \cdot G_k^r(\omega) \cdot S(R,\omega) \qquad (6)$$

The parametrization of the slip on the fault is illustrated in Figure 3. We show heterogeneous slip amplitude as varying colors for each subfault, ranging from 0.6 meters in all four corners up to 3.2 meters in the eastern center part of the fault, i.e. one of the 4 subfaults closest to the hypocenter (yellow star). Because rupture velocity (2700m/s) and rise time (0.8s) are homogeneous across the fault, it is sufficient to state the single values, which are valid for the entire fault. We add Gaussian noise to all synthetic seismograms to render our synthetic study more realistic. Because we calculate velocity and rotation rate seismograms individually, the noise on both data types is not correlated. We set the noise level to 10% of the maximum amplitude observed in all recordings for each respective data type for all scenarios. This ensures that a potential increase or decrease in inversion quality does not result from different noise levels.

We compare the inversions for two different fault mechanisms. For *Scenario I* we choose a pure left-lateral strike-slip event (rake parallel in strike direction). For *Scenario II*, its dip is changed from 90° to 45° and the sliding now occurs perpendicular to strike direction (rake $\lambda = -90°$). The fault shows pure dip-slip behavior and fractures also in vertical direction (Figure 1).

4 Energy Ratios And Amplitudes

If we compute the total energy in all three rotational components measured at all stations, the rotation rates in the horizontal components make up a very large part for the dip-slip fault (57%), whereas the strike-slip fault features the highest rotation rate ratio in the vertical components(40% for rotations around both horizontal axes), but horizontal rotation only contributes 20% of the total energy. This makes sense, since we created our strike-slip earthquake to solely rupture in horizontal direction.

To better assess the relevance of this study we check if the synthetic absolute rotation rates are in a range where they can be measured by state-of-the-art measurement devices. We therefore calculate the maximum amplitude for all 44 receivers for each of the three rotation rate components. They are shown in Figure 4.

The logarithmic scale for the rotation rates on the x-axes helps to get a sense for the amplitudes' order of magnitude. The distribution in each plot shows how all 44 amplitude values (each for one receiver) are ranging approximately between 10^{-7} and 10^{-4} rad/s. Fiber optic techniques that are able to measure these kind of horizontal-component rotations are currently under development (Velikoseltsev et al., 2012; Schreiber et al., 2009).

5 Inversion Results

For the first inversions in each scenario, we choose to use 3-component velocity seismograms from all 44 stations. To reasonably compare the inversions with and without rotation rate data, we use only half of the stations (22) for the second inversion.

With 6-component (three velocity, three rotation rate) stations, the same number of seismograms (132) will be used for both inversions. The stations in the second inversions have been selected regularly (every second one) to achieve the lowest azimuthal gap possible.

Our third analysis consists of a statistical evaluation of 200 inversions, each with a randomly selected set of receivers, for both

5 mechanisms. Since our previous results are achieved with a regular spacing of the receivers, we try to answer the question if the results are dependent on the spatial distribution of the receivers. Especially the different energy ratios of the rotation components suggest that there should be differences in the inversion results with varying station distribution.

We illustrate the results for both inversions for the 24 slip amplitudes in Figure 5. Each panel represents a subfault with the same arrangement as in Figure 2. In each panel the homogeneous *prior pdf* is drawn as a black dashed line and the true value

10 for the slip in meters in each subfault is marked with a red line. The *posterior pdf* for the 3C inversion is drawn as a solid black line, the one for the 6C inversion in blue. We calculate the information gain for each parameter, i.e. for each subfault, individually. These values, in units of bit, are also printed in Figure 5 in the corresponding colours (black/blue) for the 3C/6C inversion. We see that the results clearly vary with depth. Not only does the cumulative information gain for the 3C and 6C inversion decrease the deeper the subfault is buried (top row: 4.86 bit(3C), 5.81 bit(6C); middle row: 4.47 bit(3C) 4.80 bit(6C);

15 bottom row: 4.31 bit(3C), 4.37 bit(6C)), but also the percentage of how much the information gain increased in the 6C inversion compared to the 3C inversion decreases with increasing depth (Table 1). This indicates that shallower subfaults are resolved better in the inversion and rotation rates are likely to improve these subfaults more than deeper subfaults. It seems like the bottom row of the subfaults does not show any improvement by the incorporation of rotational ground motion data. This agrees with several studies (e.g. (Bernauer et al., 2014; Cotton and Campillo, 1995; Semmane et al., 2005; Monelli and Mai, 2008;

20 Mendoza and Hartzell, 1989)). The total cumulative information gain over all 24 subfaults is with 14.98bit about 9.86% larger for the 6C inversion than for the 3C inversion with 13.63bit.

We illustrate the *posterior pdf's* for the two parameters that are not linearly related to displacement, i.e. rupture velocity and rise time, in Figure 6. We use the same labelling as in Figure 5. We cannot resolve the exact true values very well, but if one compares the information gain between the 3C inversion and the 6C inversion, there is a clear increase when incorporating

25 rotation rate data into the inversion scheme. There is a 45.02% increase in information gain for inverting for rupture velocity and a 17.77% increase for inverting for rise time. This is again in agreement with the results from (Bernauer et al., 2014) where the true values are also not captured and the increase in information gain is around the same order for both values.

In Figure 7 we illustrate the results for a dip-slip fault in the same manner as Figure 5. The decrease of inversion quality with depth is clearly visible again. A comparison between the cumulative information gain per row leads us to the assumption that

30 slip amplitudes in the shallowest subfault layer seem well resolved whereas the deeper layers tend to be poorly resolved in the inversion process (top row: 5.18 bit(3C), 7.87 bit(6C); middle row: 4.77 bit(3C) 5.78 bit(6C); bottom row: 4.50 bit(3C), 5.43 bit(6C)). We use these numbers to calculate the increase in information gain for the 6C inversion for each row (Table 1). The highest increase can be seen in the top row. The bottom row features only a little less increase than the row above. There is a much larger difference in the middle and the bottom row for a strike-slip fault. This information tells us that for a normal fault,

35 we are able to improve the inversion quality for the parameters of the deeper parts of the fault much better than in *Scenario I* by

incorporating rotation ground motion data. The 6C inversion *posterior pdf* also seems to capture the true slip values quite well, especially on the sides and corners of the fault, compared to the results for a strike-slip fault. The total cumulative increase in information gain for all 24 subfaults is with a value of 32.13% more than three times higher than in *Scenario I*. The results for rupture velocity and rise time for a dip-slip fault are presented in Figure 8. Although we see a clear improvement between 3C

5   and 6C *posterior pdf's*, both parameters are not captured correctly by the inversions. There is, nevertheless, an improvement in resolving the true value with the 6C inversions. Especially for the rise time, the maximum of the *posterior pdf* is closer to the true value than for the 3C inversion.

The increase in information gain for rupture velocity (56.02%) and for rise time (28.47%) is also higher for *Scenario II* than for *Scenario I*.

10   The 6C inversions in the previous chapters are carried out with a manually predefined station selection.

The unequal distribution of energy ratios of rotation rate components might lead to the assumption that there is a higher information gain for the 6C inversion in *Scenario II*, because more receivers are selected north and south of the fault than in east and west direction. These receivers feature a higher energy ratio of the horizontal rotation components. To minimize this factor we run 200 6C inversions with 22 random stations each inversion, for both faulting types, and we show the results in Figure 9.

15   The results for a strike-slip fault are shown in the left column and for a dip-slip fault in the right column. We look on the slip for the top, middle and bottom row individually to better assess the inversion quality dependence with depth for the different scenarios. Therefore there are 5 histograms for the information gain for the 200 6C inversions. We mark the information gain value for the 3C inversion for each scenario with a red vertical line in the histogram plots. Slip (in gray), rupture velocity (in blue) and rise time (in green) are all colored differently to distinguish between the three types of parameters.

20   (1) For the top layer of the subfaults, the information gain for a dip-slip fault (right) reaches the highest values, which is also the result from the previous inversion. There are some receiver selections that even increase the information gain compared to the results from the inversion with regular receiver spacing.

(2) The middle subfault layer already features a smaller variance in the information gain distribution for both faulting types. We also see a decrease in information gain increase, compared to the top layer, which is to be expected from the results before.

25   Additionally, there is a higher information gain increase for a dip-slip fault (right).

(3) The deepest layer of subfaults shows the same information gain for 3C and 6C inversions for a strike-slip fault (left). The Figure shows that including rotational ground motion does not contribute to improving the results for the slip on the bottom row. This is different for a dip-slip fault (right). Every inversion increases the information gain for slip amplitudes in the bottom layer. We see some inversions in which the information gain doubles compared to the 3C inversion. This major difference in the

30   two scenarios is one of the key aspects of our results. The ability to invert for the slip amplitudes at higher depth is something that we only achieve with the incorporation of rotational ground motion rate data into the inversion. The statistical evaluation of 200 inversions with varying receiver consolidates this.

(4) The inversions for rupture velocity result in a higher information gain for a dip-slip fault, even with random station distribution. Although inversions for rupture velocity for a strike-slip event (*Scenario I*) already benefit from rotation rate data, the

35   improvement is even higher for a dip-slip (*Scenario II*) event.

(5) The incorporation of rotation rate data only slightly improves the information gain for a strike-slip fault when inverting for rise time. The randomization of the receiver distribution decreases the information gain compared to the results from the inversion with a regular receiver spacing (1.41bit) for most of the inversions. The increase in information gain for a dip-slip fault is higher.

5   We compare the results for both types of faulting in Figure 9 and see that for every row (all five parameters) the increase in information gain between 3C and 6C inversions is higher for a pure dip-slip event. The random selection of the receivers used in the inversions does not undo this result.

For the dip-slip mechanism, the inversion quality depends much more on the spatial distribution of stations (larger spreading in Figure 9). This means, that much more care needs to be taken when choosing locations with respect to the fault geometry

10   for rotational sensors compared to translational sensors.

6   Discussion

With the range of measured rotational ground motions between 10^{-7} and 10^{-4} rad/s we are able to draw practical conclusions from this synthetic study since effects in this range should be observable soon (Schreiber et al., 2009).

We show a summary of the improvement of the information gain between the different scenarios and parameters in percent in

15   Table 1. Subfaults are analysed by the three horizontal layers (varying depth). The largest difference in increase in information gain for the slip amplitudes is in the deepest subfault layers. Rupture velocity and rise time benefit from rotation rate data for both types of scenarios, but the improvement is larger for the dip-slip event. The results for slip, rupture velocity and rise time are also on the same order as the results in (Bernauer et al., 2014) for a similar strike-slip event.

Rotation data seem to be most beneficial for kinematic parameters of sources that fracture at least partly in vertical direction.

20   Additionally, the increase in information gain for rupture velocity and rise time suggests possible improvements in inversions for other seismological research areas. These parameters are important for rheology and friction laws used in dynamic rupture simulations (Tinti et al., 2009). Directivity measurements could also benefit from high-quality rupture velocity inversions (Somerville et al., 1997). Rotation rate data improved the inversions for the rise time as a parameter of the source time function. This helps when working with far-field ground displacements which are related to the derivative of the source time function.

25   A successful decrease in non-uniqueness in probabilistic finite source inversion suggests manufacturing portable rotation sensors with the mentioned sensitivities. The noise level, which was set to be equal to the noise level for translational ground motions sensors of 10%, should not exceed this to successfully improve inversion results (Bernauer et al., 2014).

7   Conclusion

Overall, non-uniqueness, which is an eminent problem in inversion theory, has been significantly reduced by the incorporation

30   of synthetic rotational ground motion data.

The results from this study clearly suggest that seismological studies can benefit from the ability of seismometers to also

measure rotational ground motions in addition to the conventional three translational components. This applies not only to finite source inversions, which are a crucial part of seismological research, but probably to all work that relies on data recorded by seismic receivers for treating/inverting real earthquakes and suffers problems such as non-uniqueness due to the non-linearity of the problem.

5   We successfully showed how rotation rate measurements can reduce the degree of non-uniqueness in probabilistic finite source inversion. This is most prominent for an earthquake which also fractures in vertical direction, due to the higher energy in the horizontal rotation components. It is very likely that the vertical displacement gradient, included in these components, leads to the observed decrease in non-uniqueness since this information can not be obtained with translation recordings on the Earth's surface.

10   *Acknowledgements.* We would like to thank Lion Krischer for the support in professional code optimization. The authors acknowledge funding from the ERC advanced project ROMY (http://romy-erc.eu/). Further information necessary to replicate and build upon the reported research is available via correspondance by email.

References

Aki, K. and Richards, P.: Quantitative seismology, vol. 1, University Science Books, 2002.

Bernauer, F., Wassermann, J., and Igel, H.: Rotational sensors—a comparison of different sensor types, Journal of seismology, 16, 595–602, 2012.

Bernauer, M., Fichtner, A., and Igel, H.: Reducing nonuniqueness in finite source inversion using rotational ground motions, Journal of Geophysical Research: Solid Earth, 119, 4860–4875, 2014.

Cotton, F. and Campillo, M.: Frequency domain inversion of strong motions: application to the 1992 Landers earthquake, Journal of Geophysical Research: Solid Earth (1978–2012), 100, 3961–3975, 1995.

DeSalvo, R.: Review: accelerometer development for use in gravitational wave-detection interferometers, Bulletin of the Seismological Society of America, 99, 990–997, 2009.

Fichtner, A. and Igel, H.: Sensitivity densities for rotational ground-motion measurements, Bulletin of the Seismological Society of America, 99, 1302–1314, 2009.

Fichtner, A. and Tkalčić, H.: Insights into the kinematics of a volcanic caldera drop: Probabilistic finite-source inversion of the 1996 Bardarbunga, Iceland, earthquake, Earth and Planetary Science Letters, 297, 607–615, 2010.

Igel, H., Cochard, A., Wassermann, J., Flaws, A., Schreiber, U., Velikoseltsev, A., and Dinh, N.: Broad-band observations of earthquake-induced rotational ground motions, Geophysical Journal International, 168, 182–196, 2007.

Kennett, B., Engdahl, E., and Buland, R.: Constraints on seismic velocities in the Earth from traveltimes, Geophysical Journal International, 122, 108–124, 1995.

Lantz, B., Schofield, R., O'Reilly, B., Clark, D., and DeBra, D.: Review: Requirements for a ground rotation sensor to improve Advanced LIGO, Bulletin of the Seismological Society of America, 99, 980–989, 2009.

Mendoza, C. and Hartzell, S.: Slip distribution of the 19 September 1985 Michoacan, Mexico, earthquake: Near-source and teleseismic constraints, Bulletin of the Seismological Society of America, 79, 655–669, 1989.

Monelli, D. and Mai, P.: Bayesian inference of kinematic earthquake rupture parameters through fitting of strong motion data, Geophysical Journal International, 173, 220–232, 2008.

Monelli, D., Mai, P., Jónsson, S., and Giardini, D.: Bayesian imaging of the 2000 Western Tottori (Japan) earthquake through fitting of strong motion and GPS data, Geophysical Journal International, 176, 135–150, 2009.

Mosegaard, K. and Tarantola, A.: Monte Carlo sampling of solutions to inverse problems, Journal of Geophysical Research: Solid Earth (1978–2012), 100, 12 431–12 447, 1995.

Nigbor, R.: Six-degree-of-freedom ground-motion measurement, Bulletin of the Seismological Society of America, 84, 1665–1669, 1994.

Nissen-Meyer, T., van Driel, M., Stähler, S., Hosseini, K., Hempel, S., Auer, L., Colombi, A., and Fournier, A.: AxiSEM: broadband 3-D seismic wavefields in axisymmetric media, Solid Earth, 5, 425–445, 2014.

Schreiber, K., Klügel, T., Velikoseltsev, A., Schlüter, W., Stedman, G., and Wells, J.-P.: The large ring laser G for continuous Earth rotation monitoring, Pure and applied geophysics, 166, 1485–1498, 2009.

Semmane, F., Campillo, M., and Cotton, F.: Fault location and source process of the Boumerdes, Algeria, earthquake inferred from geodetic and strong motion data, Geophysical research letters, 32, 2005.

Somerville, P., Smith, N., Graves, R., and Abrahamson, N.: Modification of empirical strong ground motion attenuation relations to include the amplitude and duration effects of rupture directivity, Seismological Research Letters, 68, 199–222, 1997.

Spudich, P., Steck, L., Hellweg, M., Fletcher, J., and Baker, L.: Transient stresses at Parkfield, California, produced by the M 7.4 Landers earthquake of June 28, 1992: Observations from the UPSAR dense seismograph array, Journal of Geophysical Research: Solid Earth (1978–2012), 100, 675–690, 1995.

Suryanto, W.: Rotational motions in seismology, theory and application, Ph.D. thesis, Ph. D. dissertation, Dep. of Earth and Environ. Sci. Geophys., Univ. of Munich, Munich, Germany, 2006.

Takeo, M.: Ground rotational motions recorded in near-source region of earthquakes, Geophysical Research Letters, 25, 789–792, 1998.

Takeo, M. and Ito, H.: What can be learned from rotational motions excited by earthquakes?, Geophysical Journal International, 129, 319–329, 1997.

Tarantola, A.: Inverse problem theory and methods for model parameter estimation, siam, 2005.

Tinti, E., Cocco, M., Fukuyama, E., and Piatanesi, A.: Dependence of slip weakening distance (Dc) on final slip during dynamic rupture of earthquakes, Geophysical Journal International, 177, 1205–1220, 2009.

Trifunac, M.: Earthquake Engineering, Non-linear Problems in, in: Encyclopedia of Complexity and Systems Science, pp. 2421–2438, Springer, 2009.

Twiss, R., Souter, B., and Unruh, J.: The effect of block rotations on the global seismic moment tensor and the patterns of seismic P and T axes, Journal of Geophysical Research: Solid Earth (1978–2012), 98, 645–674, 1993.

van Driel, M., Krischer, L., Stähler, S., Hosseini, K., and Nissen-Meyer, T.: Instaseis: instant global seismograms based on a broadband waveform database, Solid Earth Discussions, 7, 957–1005, 2015.

Velikoseltsev, A., Schreiber, K., Yankovsky, A., Wells, J.-P., Boronachin, A., and Tkachenko, A.: On the application of fiber optic gyroscopes for detection of seismic rotations, Journal of seismology, 16, 623–637, 2012.

Table 1. Increase in information gain for 6C inversions compared to 3C inversions in percent. Subfaults are analysed in the three horizontal layers (varying depth). The largest difference in information gain increase for the slip amplitude is in the deepest subfault layers. Rupture velocity and rise time benefit from rotation rate data for both types of scenarios, but the improvement is larger for the dip-slip scenario.

Parameter	Strike-Slip	Dip-Slip
Slip, overall [%]	9.86	32.13
Slip, top row [%]	19.58	52.08
Slip, middle row [%]	7.53	21.20
Slip, bottom row [%]	1.32	20.75
Rupture velocity [%]	45.02	56.02
Rise time [%]	17.77	28.47
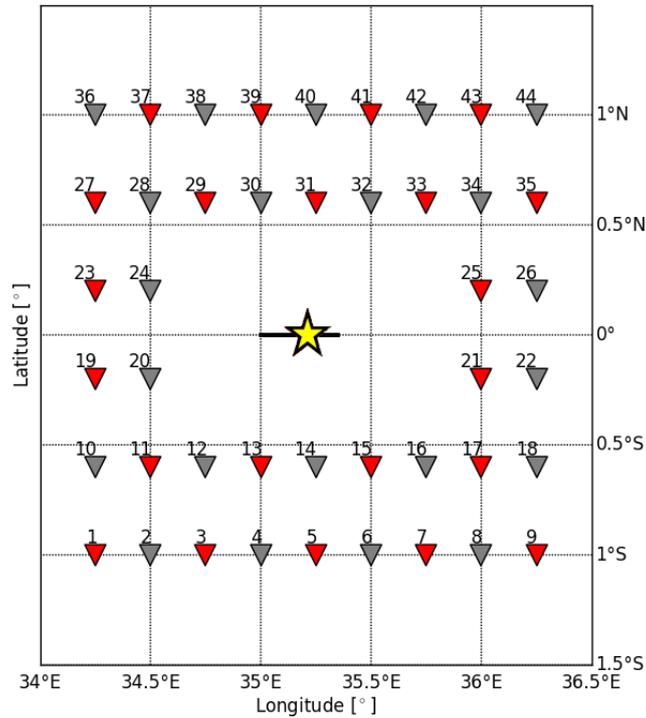
Figure 1. 44 receivers, marked as grey (only used without rotation data) and red triangles (used for all inversions) are setup around the source with a spacing of $0.4°$ latitude and $0.25°$ longitude. The fault is illustrated as a black line with constant latitude of $0°$. The yellow star marks the epicenter of the earthquake.
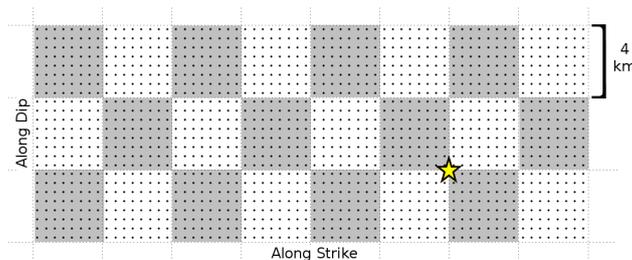
Figure 2. 2D illustration of the fault neglecting constant third dimension. The fault is broken up into 24 subfaults, each consisting of 64 point sources. Each subfault will rupture appropriately delayed in time, depending on the distance to the hypocenter. The hypocenter (marked as a yellow star) is set to be exactly between four subfaults for easier computation of the rupture times of the subfaults.
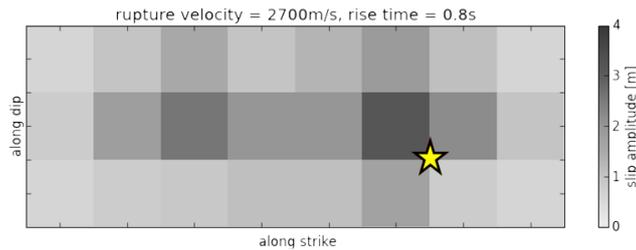
Figure 3. Illustration of the parameter space for the inversion. Rupture velocity and rise time are set to be homogeneous across the fault. There are 24 slip amplitudes, one for each subfault across the fault. The values range from 0.6m in the corners to 3.2m in one of the subfaults closest to the hypocenter (yellow star).
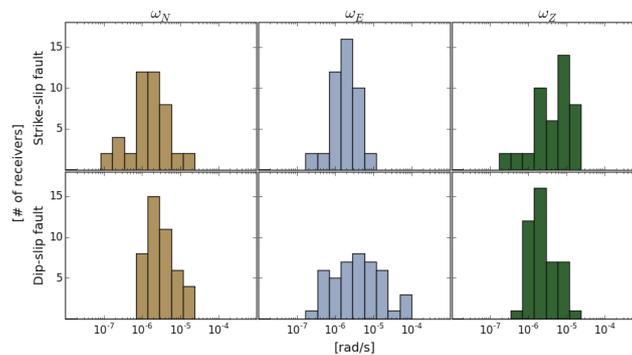
Figure 4. Histograms for maximum amplitudes of the three rotation components at all stations. The top row shows the distribution for the strike-slip fault, the bottom row for the dip-slip fault. The logarithmic scale for the rotation rates helps to get a sense for the amplitudes' order of magnitude. The histograms show how all 44 maximum amplitude values (for all 44 receivers) are ranging between 10^{-7} and 10^{-4} rad/s.
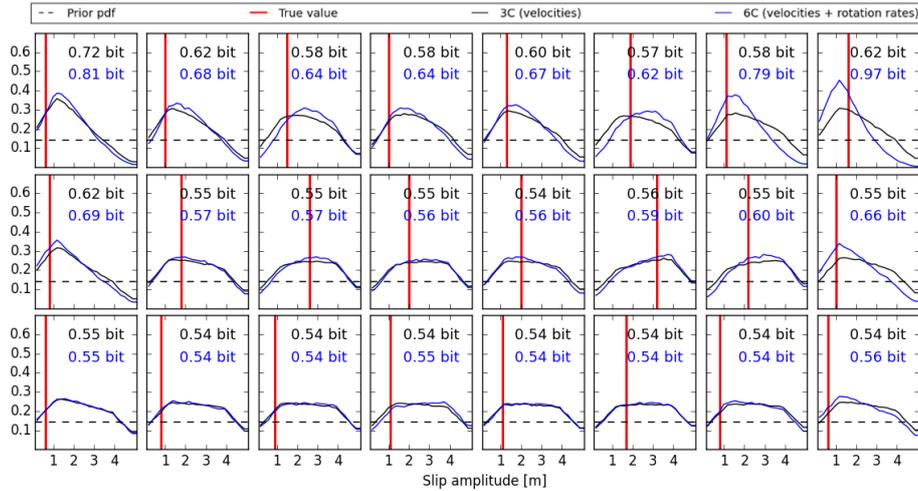
Figure 5. Inversion results for slip amplitudes for a strike-slip fault. Each panel represents a subfault with the same arrangement as in Figure 2. For each subfault, the homogeneous *prior pdf* is drawn as a black dashed line, the true value for the slip amplitudes as a red vertical line and the information gain is noted in the respective color of the inversion (3C in black and 6C in blue). The *posterior pdf's* for the 3C and 6C inversions are drawn as black respectively blue lines. The quality of the inversion shows a clear decreasing dependency with increasing depth. The bottom layer seems not to be able to be resolved better by the 6C inversion.
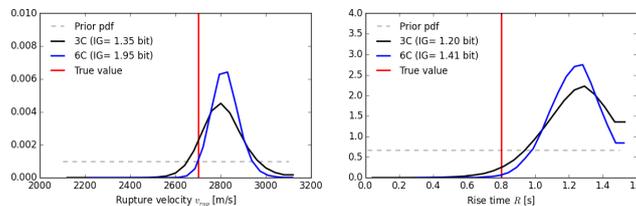
Figure 6. Inversion results for rupture velocity v_{rup} (left) and rise time R (right) for a strike-slip fault. The *prior pdf* is shown as a black dashed line, the true value as a vertical red line and the *posterior pdf* for the 3C inversion as a black line and for the 6C inversion as a blue line. The information gain increased with incorporation of rotation rate data by 45.02% for inverting for rupture velocity and by 17.77% increase for rise time. The true values are not captured better by the 6C inversion.
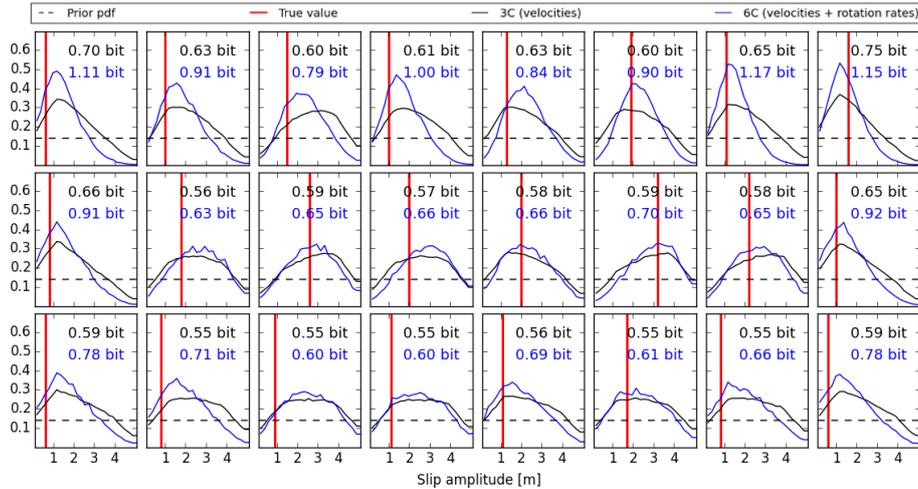
Figure 7. Inversion results for slip amplitudes for a dip-slip fault. Each panel represents a subfault with the same arrangement as in Figure 2. For each subfault, the homogeneous *prior pdf* is drawn as a black dashed line, the true value for the slip amplitudes as a red vertical line and the information gain is noted in the respective color of the inversion (3C in black and 6C in blue). The *posterior pdf's* for the 3C and 6C inversions are drawn as black respectively blue lines. The increase in information gain is higher compared to Figure 5 for all subfaults, but is still decreasing with depth.
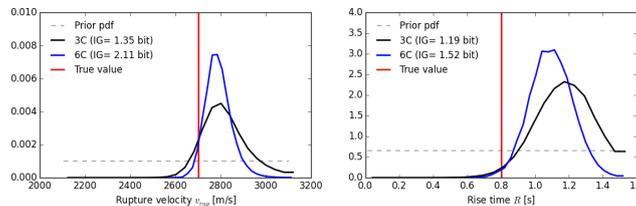
Figure 8. Inversion results for rupture velocity v_{rup} (left) and rise time R (right) for a dip-slip fault. The *prior pdf* is shown as a black dashed line, the true value as a vertical red line and the *posterior pdf* for the 3C inversion as a black line and for the 6C inversion as a blue line. The information gain increased with incorporation of rotation rate data by 56.02% for inverting for rupture velocity and by 28.47% increase for rise time. Here, in contrast to Figure 6, the true values are captured better by the 6C inversion than by the 3C inversion.
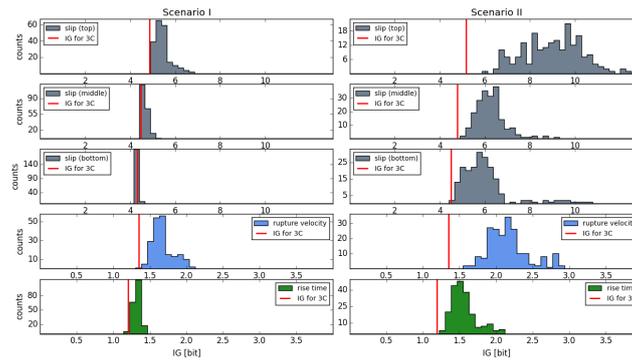
Figure 9. Histograms for the information gain for 200 inversions with random station distribution. The results for a strike-slip fault are shown in the left column and for a dip-slip fault in the right column. We add the information gain for the slip parameters row-wise to better assess the inversion quality dependence with depth. Slip (in gray), rupture velocity (in blue) and rise time (in green) are colored differently to distinguish between the three types of parameters. The statistical analysis validates the previous results. Independent of the choice of receivers (due to the random selection for each inversion) the information gain increase for the 6C inversion decreases with increasing depth and rupture velocity and rise time seem to benefit from the rotation rate data as well. Overall, the information gain increase is higher for *Scenario II*, even when randomizing the stations for the 6C inversion.